Advanced Materials

ADVANCED MATERIALS
www.advmat.de

RESEARCH ARTICLE OPEN ACCESS

White-Light Emission in Zeolitic Imidazolate Framework Glasses

Zhencai Li[1] | Zihao Wang[2] | Huotian Zhang[3] | Xuan Ge[1,4] | Ivan Hung[5] | Bozhao Yin[6] | Fengming Cao[1] | Pritam Banerjee[7] | Tianzhao Xu[1] | Lars R. Jensen[8] | Joerg Jinschek[7] | Morten M. Smedskjaer[1] | Zhehong Gan[5] | Laurent Calvez[9] | Guoping Dong[6] | Jianbei Qiu[10] | Donghong Yu[1] | Feng Gao[3] | Haomiao Zhu[2] | Yuanzheng Yue[1]

[1]Department of Chemistry and Bioscience, Aalborg University, Aalborg, Denmark | [2]Xiamen Research Center of Rare Earth Materials, Haixi Institutes, Chinese Academy of Sciences, Xiamen, China | [3]Department of Physics, Chemistry, and Biology (IFM), Linköping University, Linköping, Sweden | [4]Shanghai Key Laboratory of Materials Laser Processing and Modification, School of Materials Science and Engineering, Shanghai Jiao Tong University, Shanghai, China | [5]National High Magnetic Field Laboratory, Tallahassee, Florida, USA | [6]State Key Laboratory of Luminescent Materials and Devices, School of Materials Science and Engineering, South China University of Technology, Guangzhou, China | [7]National Centre for Nano Fabrication and Characterization (DTU Nanolab), Technical University of Denmark (DTU), Kongens Lyngby, Denmark | [8]Department of Materials and Production, Aalborg University, Aalborg, Denmark | [9]CNRS, ISCR (Institut Des Sciences Chimiques De Rennes), Univ Rennes 1, Rennes, France | [10]School of Material Science and Engineering, Kunming University of Science and Technology, Kunming, China

Correspondence: Zhencai Li (zhli@bio.aau.dk) | Haomiao Zhu (zhm@fjirsm.ac.cn) | Yuanzheng Yue (yy@bio.aau.dk)

Received: 12 December 2025 | **Revised:** 24 February 2026 | **Accepted:** 24 March 2026

Keywords: critical annealing temperature | electronic conjugation | redshift | white light emission | zeolitic imidazolate framework glasses

ABSTRACT

Some zeolitic imidazolate frameworks (ZIFs) represent a new family of glass formers, with hitherto unknown photonic functionalities. In this work, we report the discovery of broadband white light emission in ZIF-62, achieved through a vitrification-pressurization-annealing strategy. In this strategy, visible (blue) light emission was realized after the vitrification of ZIF-62, subsequently enhanced and broadened upon pressurization. Additionally, a sharp redshift (37 nm) of the emission peak occurred in pressurized ZIF-62 glass as the annealing temperature exceeded a critical annealing temperature ($1.07T_g$). This implies that the photoluminescence of ZIF-62 can be precisely tailored. The photoluminescence quantum yield of ZIF-62 glass reached 12.2% after annealing at $1.13T_g$ for 30 min. The origin of the observed phenomena was revealed by conducting structural analyses. Based on the annealed ZIF-62 glass with the best photoluminescent performance, a white light-emitting diode (LED) was fabricated, which exhibited a luminous efficacy of 4.2 lm/W and a high operational stability, i.e., retaining 36.8% of the efficacy after 72 h of operation. This work demonstrated the feasibility of the development of one-component white LEDs by utilizing the annealed ZIF-62 glass.

1 | Introduction

Solid-state white light-emitting diodes (LEDs) have emerged as an attractive solution for next-generation illumination owing to their exceptional energy efficiency, long operational lifespans, and environmental sustainability [1]. They are typically fabricated by combining a blue GaN-based LED with either a single yellow phosphor or a combination of red and green phosphors. Thus, phosphors play a crucial role in white LEDs because their performance directly determines the luminous efficacy, color rendering index (CRI), color temperature, reliability, and device lifespan [2]. Nowadays, various types of white LED phosphors have been developed, which can be classified into inorganic crystal phosphors [3], organic phosphors [4], perovskite nanocrystals [5], and inorganic glass/ceramic-based phosphors [6, 7]. Each phosphor has achieved impressive performance along many

dimensions but suffers from distinct limitations, such as poor moisture resistance and low chemical stability. To overcome these limitations, it is crucial to develop novel luminescent zeolitic imidazolate frameworks (ZIFs), a subset of metal–organic frameworks (MOFs), as white light phosphors [8, 9].

MOFs are microporous crystals composed of metal ions coordinated to organic ligands, possessing a large surface area that enables various applications in gas sorption [10–12], gas separation [13], catalysis [14], and ion transportation [15]. Some ZIFs can be vitrified to the glass state via melt-quenching, with their porosity being inherited from the crystal state to a great extent [16, 17]. For instance, ZIF-4 ($M(Im)_2$) and ZIF-62 ($M(Im)_{2-x}(BIm)_x$) are good glass formers, where M is the central metal node such as Zn^{2+} or Co^{2+}, and Im and BIm are the linkers of imidazole ($C_3H_3N_2^-$), and benzimidazole ($C_7H_5N_2^-$), respectively. ZIF-62 demonstrates ultrahigh glass-forming ability and a wide temperature window of molten state between its liquidus and decomposition temperatures [18, 19]. Thus, ZIF-62 can be readily vitrified using the spark plasma sintering (SPS) technique to produce hot-pressed ZIF-62 glass [20]. Owing to the $3d^{10}$ close-shell configuration of Zn, Zn-based ZIF crystals have been considered photoluminescent-inactive in the visible regions [21]. However, given that both Im and BIm show luminescence due to their outstanding optical absorption and π–π^* electronic transition in *p*-orbital [22], the Zn-based ZIF-62 crystal is expected to exhibit luminescent properties that differ from those of its linkers. Its luminescence behavior should depend on π–π^* transition in *p*-orbital of the linkers and ligand-to-ligand charge transfer (LLCT). Nevertheless, the ZIF-62 crystal only exhibits strong ultraviolet light emission from π–π^* transition in the linkers, but not visible-light emission from LLCT, because of its wide bandgap (around 3.58 eV). Therefore, the ZIF-62 crystal is not considered a white light phosphor.

In this work, we first discovered that vitrification-pressurization-annealing of ZIF-62 crystals enables white-light emission. Specifically, the vitrification of ZIF-62 crystals enabled broadband blue-light emission, and subsequent annealing of the ZIF-62 glasses facilitated the generation of broadband white-light emission, distinctly different from that observed in the ZIF-62 crystals. Moreover, the broadband blue-light emission of ZIF-62 glass was significantly enhanced by annealing at $1.07T_g$ (where T_g is the glass transition temperature), and simultaneously, a redshift was induced. We clarified the structural and electronic origin of both the emission enhancement and the redshift. Finally, we succeeded in fabricating ZIF-62 glass-based white LEDs with high photoluminescence quantum yield (PLQY) and good thermal stability.

2 | Results and Discussion

2.1 | Characterizations of ZIF-62 and Glasses

Figure 1a shows the schematic unit cell structure of a ZIF-62 crystal. The synthesized ZIF-62 was used for fabricating melt-quenched ZIF-62 glass (MQG) [23, 24]. Then, hot-pressed glass (HPG) was obtained by subjecting the MQG to the SPS process. Both HPG and MQG (in tablet form) were annealed at various temperatures above their T_g, noted as $HPG_{xxx\text{-}yy}$ and $MQG_{xxx\text{-}yy}$, where *xxx* denotes the annealing temperature (in K) and *yy* refers to the annealing time (in min), respectively. Figure 1b illustrates the preparation procedure of the studied samples, along with their optical images under natural light. Their characteristics are shown in Tables S1 and S2, where their chemical compositions were determined through liquid ^1H NMR spectroscopy (Figure S1), their crystalline or amorphous structure was identified from the X-ray diffraction (XRD) analysis (Figure 1d), and T_g and melting point (T_m) were determined from the differential scanning calorimetry (DSC) curves in Figure 1c.

The endotherm (440–600 K) in the DSC upscan curve of ZIF-62 crystal (Figure 1c) is caused by the desolvation of DMF, whereas the endotherm (between 684 and 719 K) is due to melting [16]. Upon hot-pressing (HP) at 60 MPa, the T_g of MQG decreases from 593 K to around 550 K. This decrease was attributed to the pressure-induced weakening of the intermediate-range structural connectivity [18]. Upon annealing at 673 K (i.e., 80 K above ambient pressure T_g) for 30 min, T_g of HPG increases to around 563 K, implying that the partially distorted structure recovers to a more thermodynamically stable state (Figure S2). The XRD patterns (Figure 1d) and the high-energy synchrotron XRD (HEXRD) patterns (Figure S3a) confirm the crystalline nature of ZIF-62 and the non-crystalline nature of MQG, HPG, and $HPG_{673\text{-}30}$ samples. Further, the XRD patterns (Figure S3b) prove that HPG annealed at various temperatures remains glassy. The tetrahedral Raman active vibrations in ZIF-62, MQG, HPG, and $HPG_{673\text{-}30}$ samples occur at nearly the same frequencies with similar amplitude (Figure 1e), confirming that the organic ligands remain intact in the glass state [18, 25]. However, compared to the Zn—N stretching modes of crystalline ZIF-62, those of the three glasses slightly shift to a higher frequency, while the C—N stretching modes shift to a lower frequency, indicating the vitrification-induced distortion in the tetrahedral network (Figure S4a,b,d) [20]. These adjustments make Z—N bonds stronger and C—N bonds weaker compared to ZIF-62. Interestingly, the three treated glasses exhibit stronger fluorescence than that of crystalline ZIF-62, with $HPG_{673\text{-}30}$ featuring the strongest fluorescence. This highlights the significant impact of the subtle tetrahedral rearrangement on the electronic structure of the glasses (Figure S4c), leading to enhanced photoluminescence (PL). We characterize the crystal-to-glass transition of ZIF-62 by in situ heating transmission electron microscopy (TEM). The morphologies of ZIF-62, MQG, and $MQG_{673\text{-}30}$ samples are shown in the first column in Figure S5a–c, respectively. The selected area electron diffraction (SAED) patterns (second column in Figure S5a–c) confirm the ordered structure of ZIF-62 crystal and the disordered structure of MQG and $MQG_{673\text{-}30}$, respectively [26]. Energy dispersive X-ray spectroscopy mapping analysis, as collected from the high-angle annular dark-field imaging scanning TEM images, confirms the homogeneous distribution of Zn, C, and N elements in the samples (the fourth, fifth, and sixth columns in Figure S5a–c).

2.2 | Photoluminescence Performance of ZIF-62 Crystal and Glasses

Figure 2a–d shows the 2D (excitation-emission) fluorescence spectra of ZIF-62, MQG, HPG, and $HPG_{673\text{-}30}$, respectively. ZIF-62 exhibits a narrow emission peak at 300 nm under excitation at the wavelength of 250 nm (Figure S6a) and extremely weak

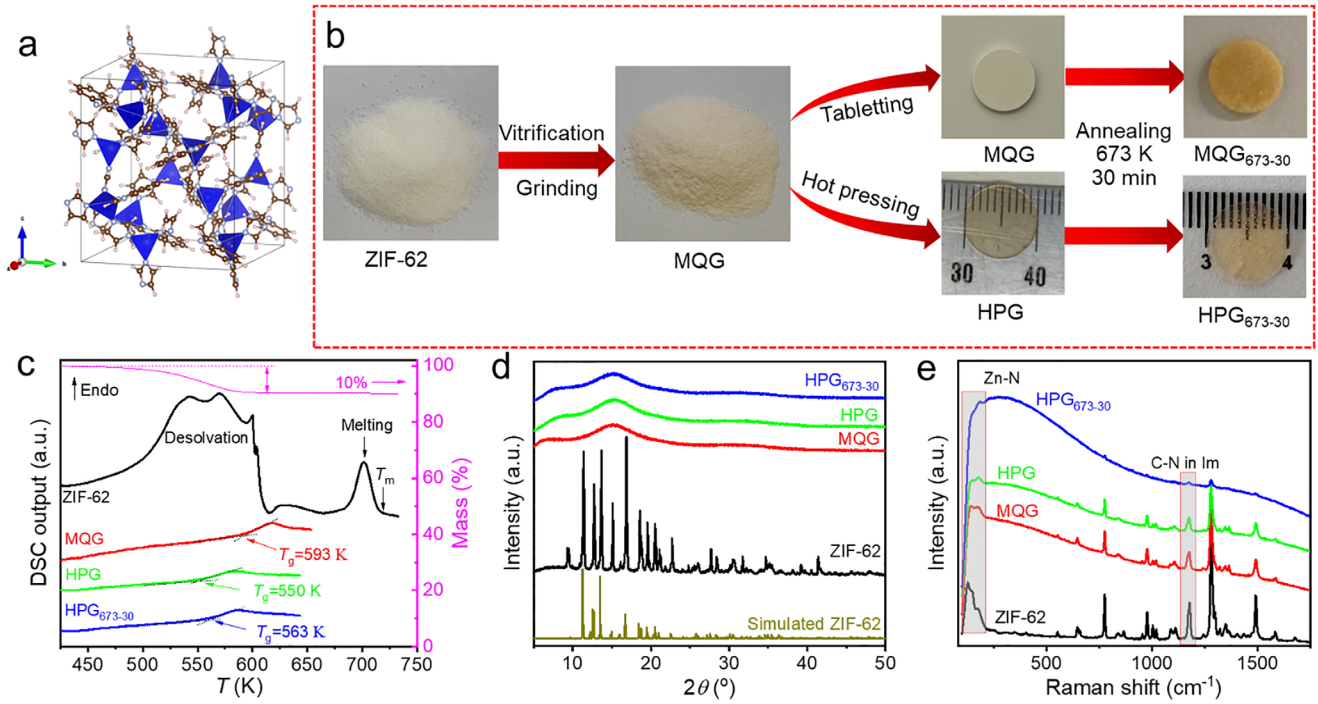

FIGURE 1 | Synthesis and characterization of ZIF-62 crystal and glasses. (a) Unit cell structure of ZIF-62 crystal. (b) Flow chart of melting applied to ZIF-62, hot-pressing (HP) applied to melt-quenched glass (MQG) powder, tableting, and annealing applied to MQG, and annealing applied to hot-pressed glass (HPG). (c) Thermogravimetric curve (magenta color) of ZIF-62 crystal and DSC curves of ZIF-62, MQG, HPG, and $HPG_{673\text{-}30}$. (d) XRD patterns of simulated ZIF-62, ZIF-62, MQG, HPG, and $HPG_{673\text{-}30}$. (e) Raman spectra of ZIF-62, MQG, HPG, and $HPG_{673\text{-}30}$.

broad emission peaks at around 400–600 nm under excitation at 320, 370, and 410 nm (Figure S6b–d). Interestingly, the weak broad emissions are strongly enhanced and red-shifted through vitrification, HP, and annealing at 673 K for 30 min (Figure 2b–d; Figure S6b–d). However, the narrow peak of native ZIF-62 weakens with vitrification, HP, and annealing at 673 K for 30 min, which is attributed to the lack of periodic arrangement of Im/BIm rings (structural disorder), suppressing π^*-π transitions in Im/BIm rings (Figure 2e; Figure S7a,b). In addition, the narrow emission peak of ZIF-62 exhibits a slight blueshift (to a shorter wavelength) upon vitrification, HP, and annealing at 673 K for 30 min (Figure S6). This blueshift could result from the scission and renewal of some Zn—N coordination bonds during vitrification and HP, leading to a distortion of tetrahedral units in MQG and HPG [27]. The enhancement of the broad emission peaks is assigned to the enhanced possibility of LLCT in the framework. The red-shifting of the broad emission peaks in the annealed HPG and $HPG_{673\text{-}30}$ can be attributed to LLCT induced red-edge effect [28], leading to an increase of electron population in the lower energy level of the π–π^* molecular orbitals in Im/BIm rings. Their emission positions coincide with the edge position of their absorption spectra (Figure S8a–c) [29]. The proposed energy transfer process (redshifting) of the PL in ZIF-62, MQG, HPG, and $HPG_{673\text{-}30}$ is shown in Figure 2e. Upon excitation <300 nm, the electrons at the ground state level (S_0) are jumped to the excited state level (S_1) in the ZIF-62 crystal. Then the electrons at S_1 return to S_0, resulting in a light emission at 300 nm. Upon melt-quenching, hot-pressing, and annealing at 673 K, the structural network in ZIF-62 is distorted at both short-and medium-length scales [20], leading to the splitting of the excited state level (S_1) into multiple lower-energy sublevels such as S_2 and S_3. The number of spheres represents the photon population at the corresponding energy levels. Such enhancement and redshift also appear at both MQG and HPG samples annealed at lower temperatures (Figures S9 and S10).

The optical images in Figure 2f illustrate the emission colors of ZIF-62, HPG, and $HPG_{673\text{-}30}$ under excitation of 365 nm laser. Upon vitrification, HP, and annealing at 673 K for 30 min, the broad emission of ZIF-62 is significantly enhanced, accompanied by a color shift from blue to cold-white. These results indicate that the $HPG_{673\text{-}30}$ is a highly promising candidate for application in white LEDs. The chromaticity coordinates of ZIF-62 (0.210, 0.216), MQG (0.195, 0.179), HPG (0.205, 0.202), and $HPG_{673\text{-}30}$ (0.256, 0.295) under 370 nm excitation are marked in the CIE 1931 color spaces (Figure 2g). The color point of $HPG_{673\text{-}30}$ lies in the cold-white lighting region, whereas those of ZIF-62, MQG, and HPG are in the blue lighting region. The chromaticity coordinates of ZIF-62, MQG, HPG, and $HPG_{673\text{-}30}$ under 250, 320, and 410 nm excitation are shown in Figure S11. We find that ZIF-62, MQG, HPG, and $HPG_{673\text{-}30}$ emit much weaker cold-white light under 250 nm excitation compared to other excitation wavelengths (Figure S6). Therefore, $HPG_{673\text{-}30}$ is regarded as an excellent candidate for cold-white light emitting under 370 nm excitation.

Figure 2h and Table S3 show the absolute internal PLQY values for ZIF-62, MQG, HPG, and $HPG_{673\text{-}30}$ under excitation at 280, 320, 365, and 405 nm, respectively. The internal PLQY of ZIF-62 under excitation at 280 nm sharply decreases from 4.52% to 1.75% upon vitrification, hot-pressing, and annealing at 673 K for 30 min. In contrast, the internal PLQY of ZIF-62 crystal under excitation at 320 nm first increases from 3.32% to 11.74% upon

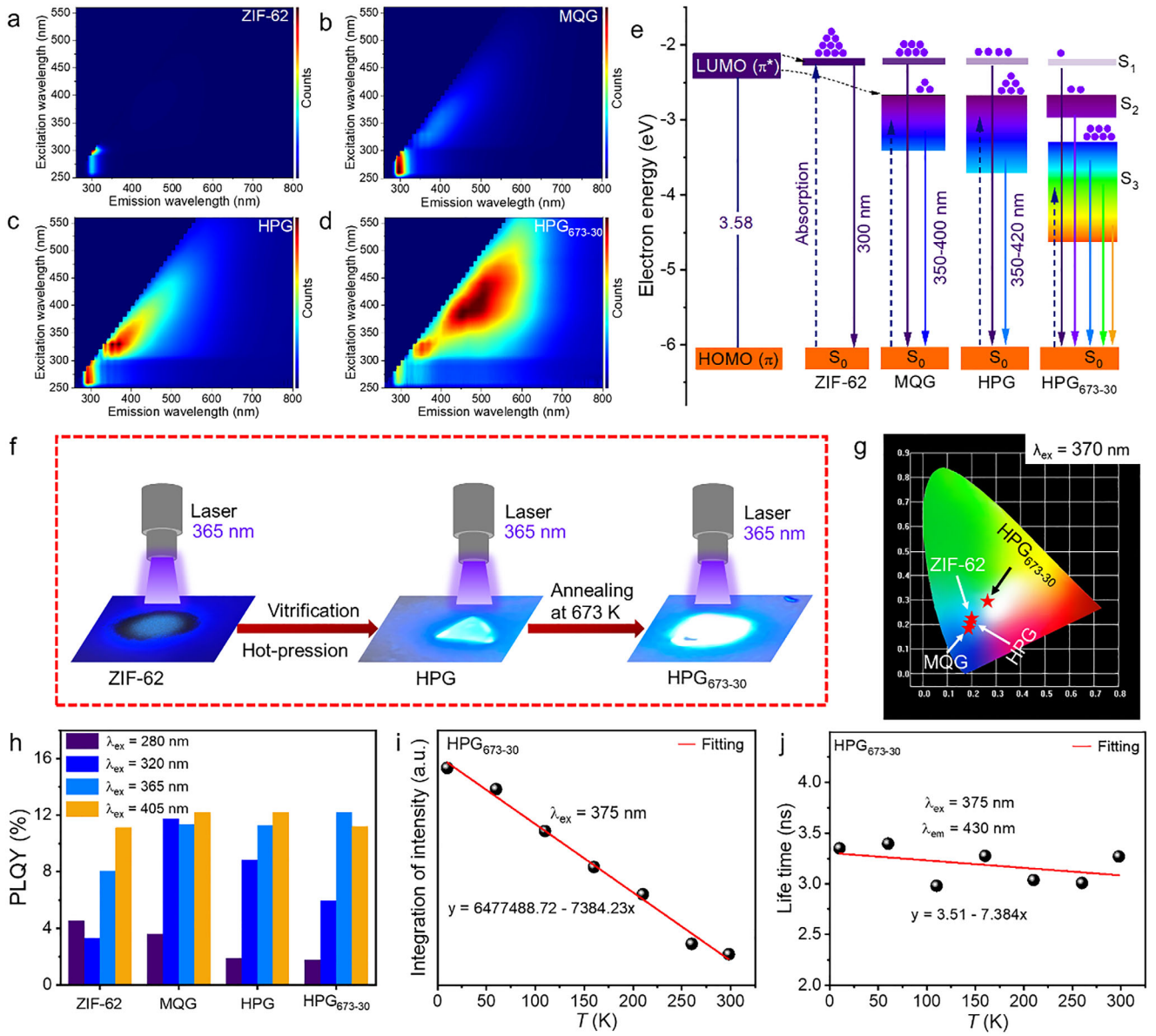

FIGURE 2 | Photoluminescence (PL) performance of ZIF-62 crystal and glasses. (a–d) 2D fluorescence (excitation/emission) spectra of (a) ZIF-62, (b) MQG, (c) HPG, and (d) $HPG_{673\text{-}30}$. (e) Schematic of proposed energy transfer process of ZIF-62, MQG, HPG, and $HPG_{673\text{-}30}$. The number of spheres represents the photon population at the corresponding energy levels. (f) Optical images of ZIF-62, HPG, and $HPG_{673\text{-}30}$ under 365 nm laser. (g) Commission Internationale de l'E´clairage (CIE) chromaticity coordinates of PL spectra of ZIF-62, MQG, HPG, and $HPG_{673\text{-}30}$ under 370 nm excitation. (h) Absolute PLQY of ZIF-62, MQG, HPG, and $HPG_{673\text{-}30}$ under excitation at 280, 320, 365, and 405 nm, respectively. (i,j) Temperature-dependent integral PL (i) and lifetime (j) of $HPG_{673\text{-}30}$ under excitation of 375 nm. The curves represent linear fits as a function of temperature.

vitrification and then decreases to 5.94% by hot-pressing and annealing at 673 K for 30 min. Evidently, it is enhanced from 8.04% to 12.19% upon vitrification, hot-pressing, and annealing at 673 K for 30 min for ZIF-62 under excitation at 365 nm. However, it remains nearly unchanged (around 12%) in ZIF-62, MQG, HPG, and $HPG_{673\text{-}30}$ under excitation at 405 nm. Similarly, the external PLQY under 365 nm excitation (Table S4) is enhanced in ZIF-62 upon vitrification, HP, and annealing at 673 K for 30 min. The fluorescence lifetime for ZIF-62 at 430 nm under excitation at 375 nm (Figure S12) is extended by vitrification, HP, and annealing at 673 K for 30 min.

Additionally, we find that the PL intensity of $HPG_{673\text{-}30}$ decreases with increasing measurement temperature (Figure S13), due to the increased possibility of non-radiative transition. By integrating the PL over the wavelength, we find that the integrated value linearly decreases with temperature (Figure 2i). Similarly, the fluorescence lifetime of emission at 430 nm for $HPG_{673\text{-}30}$ linearly decreases with increasing temperature (Figure 2j). This temperature-dependent PL and lifetime behavior indicate that $MQG_{673\text{-}30}$ (Figure S14) also exhibits excellent thermal stability in the typical operating temperature window of LEDs (around 400 K).

TABLE 1 | Photoelectric parameters for three fabricated LEDs (LED-1, -2, and -3) and a commercial white LED (CWLED) fabricated via combining an ultraviolet (365 nm) chip.

Device	CCT (K)	R_a	Chromaticity coordinate		Current (mA)	Efficacy (lm/W)	
			x	y			
LED-1	48 180	85.2	0.231	0.254	60	1.91	This work
LED-2	12 382	81.8	0.254	0.300	60	4.22	This work
LED-3	8448	91.8	0.294	0.293	100	3.15	This work
CWLED	>7000	68	0.35	0.39		110	Ref. [3]

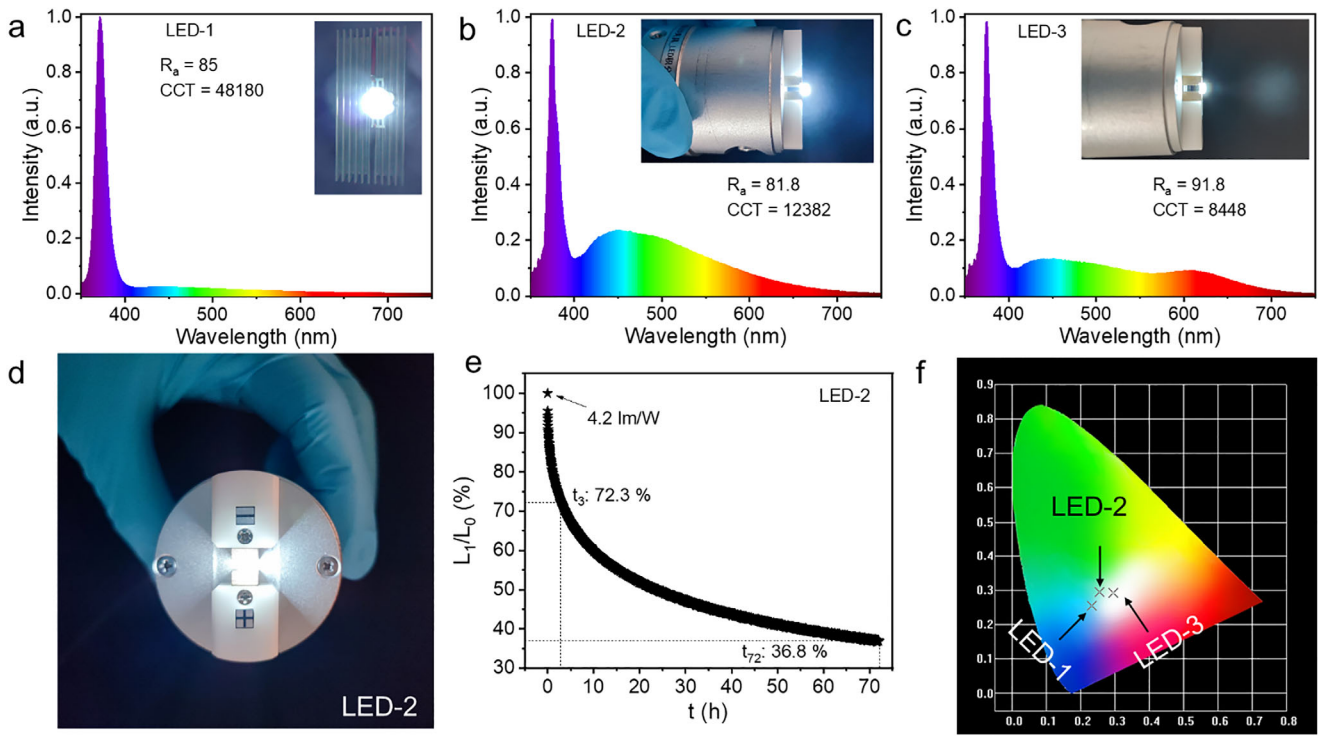

FIGURE 3 | Device performance of fabricated white LEDs based on ZIF-62 glasses. (a,b) PL spectra of LED-1 (a) and LED-2 (b) under 60 mV driving current, with photographs of the lighted LEDs shown in the insets. (c) PL spectrum of LED-3 (made by adding the commercial red phosphor ($CaAlSiN_3$:Eu^{2+})) under 100 mV driving current. (d) Photograph of LED-2. (e) Operational stability of LED-2 under continuous operation at a driving current of 60 mA. (f) Chromaticity coordinates of the three as-fabricated LEDs are marked in CIE 1931 color spaces.

2.3 | LED Performance of ZIF-62 Glasses

Based on the above-reported promising results, we fabricated six LEDs (LED-1, -2, -3, -4, -5, and -6) based on ZIF-62 glasses (see Methods Section) and evaluated their performances. Table 1 presents the photoelectric parameters of the LED-1, -2, -3, and a commercial white LED (CWLED) [3], including correlated color temperature (CCT), CRI (denoted as R_a), and luminous efficacy. Figure 3a–b shows the PL spectra of LED-1 (combining bulk HPG and a 365 nm ultraviolet chip, an LED as an excitator for exciting the LED) and LED-2 (integrating bulk $HPG_{673\text{-}30}$ and a 365 nm ultraviolet chip), respectively, under a driving current of 60 mA. The chromaticity coordinates of LED-1 (0.231 and 0.254) and LED-2 (0.254 and 0.300) appear in the blue and cold-white lighting regions in CIE 1931 (Figure 3f). The working demonstration of LED-1 and LED-2 is shown in Movies S1 and S2, respectively. Compared with the CWLED utilizing a single YAG: Ce^{3+} phosphor [30], LED-1 and LED-2 exhibit the advantage of higher R_a. However, their CCTs are significantly higher than those of CWLED, leading to a pronounced cold tone of the emitting light owing to the weak red-light component. Figure 3c shows the PL spectrum of LED-3, which is obtained under a driving current of 100 mA. Note that LED-3 is composed of bulk $HPG_{673\text{-}30}$, a 365 nm ultraviolet chip, and the commercial

red phosphor ($CaAlSiN_3$: Eu^{2+}). By introducing the commercial red phosphor into LED-3, the CCT decreases to 8448 K and R_a increases to 91.8. This indicates that a slightly warm white LED-3 is achieved under the chromaticity coordinate (0.294 and 0.293), as shown by CIE 1931 in Figure 3f, but it exhibits a much smaller luminous efficacy (3.15 lm/W) than CWLED. The luminous efficacy of the fabricated cold white LED-1 and LED-2 is also smaller than that of CWLED, respectively. It is worth noting that the luminous efficacy of LED-2 is 2.2 times higher than that of LED-1, indicating that annealing is an effective strategy to improve the luminous efficacy of ZIF-62 glass. The photographs of the lighted LED-1, LED-2, and LED-3 are shown in insets of Figure 3a–c, respectively. The zoom-in optical image of the lighted LED-2 is shown in Figure 3d, while those of the as-fabricated LED-1, LED-2, and LED-3 are shown in Figure S15. The PL spectra and photoelectric parameters of LED-4 (combining 400 nm chip and HPG), LED-5 (combining 400 nm chip and $HPG_{673\text{-}30}$), and LED-6 (combining 400 nm chip, $HPG_{673\text{-}30,}$ and commercial red phosphor) are shown in Figure S16 and Table S5, respectively. Optical images of the lighted LED-4, LED-5, and LED-6 are shown in Figure S17.

To evaluate the electric current-dependent LED performance, the PL spectra and luminous efficacies of LED-1, LED-2, LED-4, and LED-5 are measured under various driving currents from 10 to 100 mA, respectively. The luminous efficacy of the fabricated LEDs gradually decreases with increasing driving current (Figures S18–S21) due to the decrease in external quantum efficiency [31]. Figure 3e demonstrates the decay of an initial luminous efficacy (L_0) of 4.2 lm/W for LED-2 at the constant driving current of 60 mA with continuous operation time. After 3 h of continuous operation, the real working luminous efficacy (L_1) drops to 3.04 lm/W, remaining at 72.3% of L_0. After 72 h, L_1 drops to 1.54 lm/W, i.e., 36.8% of L_0. The L_1 of LED-2 decreases slowly when the operating time exceeds 3 h, implying an improved operational stability at lower L_1 values. To detect a possible structural change of HPG during LED operation at around 400 K, the initial glass was annealed at 423 K for 30 min and 9 h in atmospheric air, and subsequently was measured using the Fourier-transform infrared (FTIR) spectroscopy. The results (Figure S22) exhibit that all characteristic bands, which are associated with the vibration modes of the imidazolate/benzimidazole linkers, including the C—N stretching (1140–1500 cm^{-1}), and ring stretching modes (1500–1600 cm^{-1}), remain unchanged upon annealing. Importantly, no Zn—O vibration bands are observed, indicating that no detectable oxidation of the sample occurs during annealing. These results suggest that the LED operation temperature does not induce structural degradation of the glass, i.e., is not responsible for the decay of the luminous efficacy. However, it is still unknown whether or not the interaction between high-energy UV light and glass could induce the formation of defects (color center), and thereby cause the decay of the luminous efficacy. This will be an interesting aspect to be studied in detail.

2.4 | Structure Analysis of ZIF-62 Crystal and Glasses

To elucidate the difference in the electronic structure variations underlying the changes in PL, the atomic-scale (short-range) structure of ZIF-62 crystal and the three glasses were characterized by solid-state ^{67}Zn, ^{15}N, and ^{13}C NMR spectroscopy. Compared to ZIF-62, the ^{67}Zn NMR spectra (Figure 4a; Figure S23a) of MQG, HPG, and $HPG_{673\text{-}30}$ have broadened asymmetric line shapes with low-frequency tails, and the resonance peak shifts to a lower frequency. The broadening and characteristic line shape are attributed to a continuous distribution of C_Q due to structural disorder in the glassy state, verifying the short-range disorder of [N—Zn—N] tetrahedra in ZIF-62 glasses [32]. However, there is no detectable difference in the ^{67}Zn NMR spectra among the three ZIF-62 glasses, indicating that chemical integrity was retained upon HP and annealing. Compared to the resonance peak (around 204 ppm) for N (in Im) in the ^{15}N NMR spectrum of crystalline ZIF-62 (Figure 4b; Figure S22), those of the three glasses are broader and shifted to a higher chemical shift of 205 ppm. This reveals the ground-state deshielding effects on sigma (σ) electron clouds around nitrogen atoms, indicating that σ electron transfers from ligand (Im/BIm) to zinc metal in the three glasses [33]. This σ electron transfer is corroborated by a slight decrease in chemical shifts for Zn nuclei of MQG, HPG, and $HPG_{673\text{-}33}$ relative to that of the ZIF-62 crystal. Consequently, the σ electron between Zn and N (in Im) moves closer to the Zn nucleus upon vitrification, whereas no further movement is observed upon HP and annealing at 673 K for 30 min. This does not contribute to any π-electron conjugation effect on the redshift of the weak broadband emission in MQG [34–36]. In addition, another weak resonance peak of N (in BIm) at 190 ppm is broader in the three ZIF-62 glasses, with a slightly detectable shift in the resonance signal [37], further indicating that σ electron transfer also occurs in BIm linkers.

Similar to the ^{67}Zn and ^{15}N NMR spectra, two populations of ^{13}C are found in the ^{13}C CPMAS NMR spectra of ZIF-62, MQG, HPG, and $HPG_{673\text{-}30}$ (Figure 4c), i.e., C-nuclei in BIm and Im (insets of Figure 4c) of the ZIF-62 crystal and the three glasses. The most pronounced decreased chemical shifts are ascribed to the carbon nuclei from the imidazole units (peaks 8, 9, and 10) for the three ZIF-62 glasses compared with that for the native ZIF-62 crystal. Such lower chemical shifts correspond to increased electron density, implying possible charge transfer from N to C nuclei, resulting in charge delocalization in the linkers. The difference in ^{13}C signals indicates structural distortion of Im and BIm linkers upon vitrification, hot-pressing, and annealing. This may play a dominant role in governing the enhancement of the weak broadband emission in the three glasses.

To further probe the structural evolution of ZIF-62 caused by vitrification, hot-pressing, and annealing, HEXRD analysis is performed. The glass nature of MQG, HPG, and $HPG_{673\text{-}30}$ is verified by the lack of sharp Bragg peaks in the reciprocal-space $S(Q)$ curves (Figure 4d). Figure 4f shows that the first sharp diffraction peak (FSDP) in MQG is enhanced by HP and annealing both at 673 K for 30 min and at other temperatures (Figure S24), implying an increase in the connectivity of [N—Zn—N] tetrahedra, i.e., a higher degree of medium-range order in annealed HPG [38]. The real-space $G(r)$ data (Figure 4e) of all the samples are obtained by applying the Fourier transformation to the $S(Q)$ data. The atom-atom pair correlations of C—C(N) (1.36 Å, 1), Zn—N (2.02 Å, 2) and (4.17 Å, 4), Zn—C (3.03 Å, 3), and Zn—Zn (5.94 Å, 5) are marked in

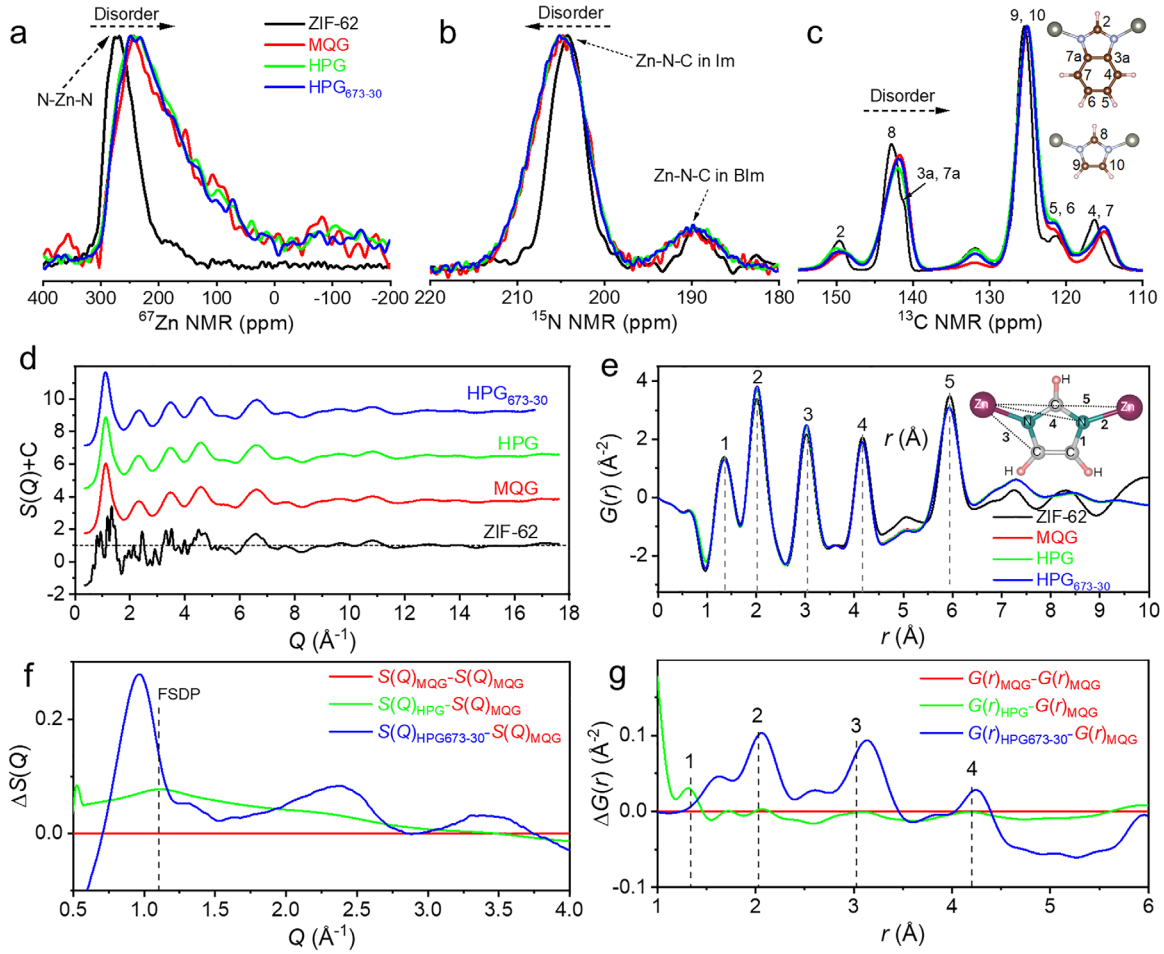

FIGURE 4 | Structure analyses of ZIF-62 and glasses. (a–c) ^{67}Zn (a), ^{15}N (b), and ^{13}C (c) MAS NMR spectra of ZIF-62, MQG, HPG, and $HPG_{673\text{-}30}$. (d) Faber-Ziman structure factors $S(Q)$ of ZIF-62, MQG, HPG, and $HPG_{673\text{-}30}$. (e) Reduced pair correlation functions $G(r)$ of ZIF-62, MQG, HPG, and $HPG_{673\text{-}30}$. (f) The differences in $S(Q)$ ($\Delta S(Q)$) of $S(Q)_{MQG}$-$S(Q)_{MQG}$, $S(Q)_{HPG}$-$S(Q)_{MQG}$, and $S(Q)_{HPG673\text{-}30}$-$S(Q)_{MQG}$. (g) The differences in $G(r)$ ($\Delta G(r)$) of $G(r)_{MQG}$-$G(r)_{MQG}$, $G(r)_{HPG}$-$G(r)_{MQG}$, and $G(r)_{HPG673\text{-}30}$-$G(r)_{MQG}$, respectively.

the $G(r)$ curves. The Zn—Zn correlation in the glasses is notably weaker than that in the crystalline counterpart, confirming that the glasses possess a higher distortion of the intermediate-range structure of Zn-linker-Zn. However, as shown in $\Delta G(r)$ curves (Figure 4g; Figure S25), the short-range correlations of C—C(N) (1.36 Å), Zn—N (2.02 Å), Zn—C (3.03 Å), and Zn—N (4.17 Å) are visually strengthened upon annealing both at 673 K for 30 min and at other temperatures. This implies that the coordination Zn—N and covalent C—C(N) bonds get strengthened through the recovery of the structural defect generated during vitrification and hot pressing.

2.5 | Mechanism of Photoluminescence in ZIF-62 Crystal and Glasses

To understand the interplay between electronic structures and PL of the studied samples, X-ray photoelectron spectroscopy (XPS) measurements are conducted for ZIF-62, MQG, and $MQG_{673\text{-}30}$. As seen in Figure S26, the peaks in Zn 2p, N 1s, and C 1s spectra of the ZIF-62 crystal become narrower through annealing. The narrowing of the XPS peaks means a more uniform electron distribution around the Zn, C, and N atoms since the recovery of the structural defect via annealing. This is confirmed by an increase in the glass network connectivity, i.e., an increase in T_g, upon annealing (Figure 1c; Figure S2a).

In addition, the electronic structure of the ZIF-62 is calculated using periodic density functional theory (PDFT) to gain insight into the PL mechanism. As shown in Figure 5a, we observe a flat band electronic structure with a bandgap of 3.58 eV. Based on the analysis of the total/partial density of states (DOS) (Figure 5b), the electronic density is mainly determined by the *p*-orbitals of C and N atoms. Furthermore, the highest occupied molecular orbital (HOMO) and the lowest unoccupied molecular orbital (LUMO) are dominated by the *p*-orbital of C and N in the Im and BIm rings (Figure S27). This indicates that the PL of ZIF-62 crystal is primarily attributed to the π–π^* interaction within the rings. The electronic structure of Im (Figure 5c) shows that 'pyridine-like' N contributes one π electron in its *p*-orbital, forming its aromaticity, while its lone-pair electrons are located in a sp^2-orbital without being involved in its molecular conjugation. The other 'pyrrole-like' N atom contributes its lone-pair electrons to the conjugated aromaticity. Therefore, the Zn—N ('pyrrole-like') coordination can influence the π electron distribution in the *p*-orbital of N, thereby affecting the PL in crystalline ZIF-62.

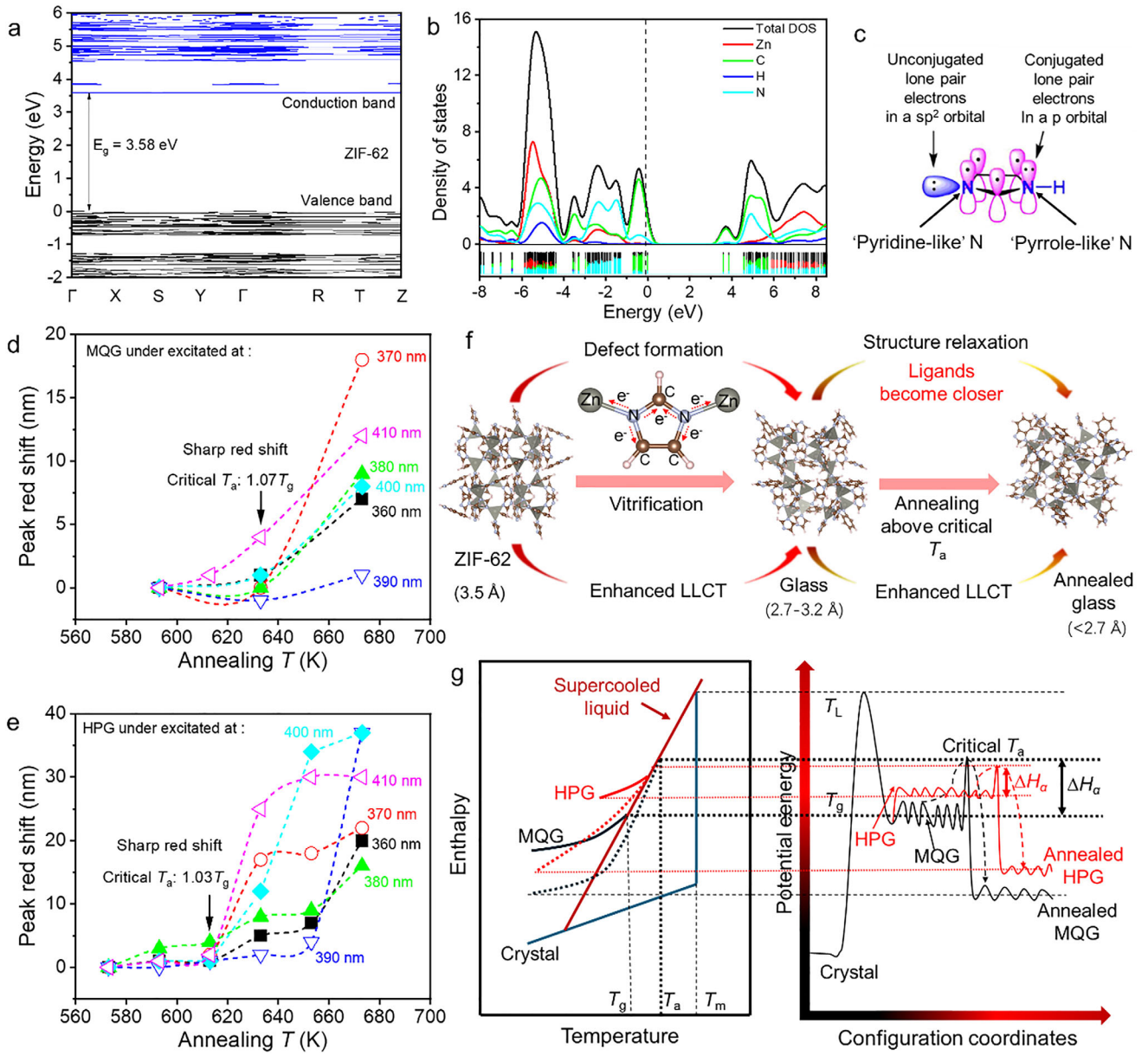

FIGURE 5 | Electrical structure and mechanism of PL in ZIF-62 crystal and glasses. (a) Band structure and (b) corresponding total/partial density of states (TDOS/PDOS) of ZIF-62. (c) Electronic structure of Im. (d,e) PL (under excitation from 360 to 410 nm) peaks redshift as a function of annealing temperature for 30 min in MQG (d) and HPG (e), respectively. (g) Schematic representation of the enthalpy relaxation from ZIF-62 melting-liquid toward a MQG cooled at the standard rate of 10 K/min (left panel) and the reflection of such relaxation on the potential energy landscape (PEL) (right panel).

In addition, the Zn—N ('pyrrole-like') bonds in crystalline ZIF-62 are expected to require lower energy barriers for the "free-rotation" during vitrification. The weak Zn—N ('pyrrole-like') bond involves delocalizing the π-lone pair electrons of N to Zn, therefore increasing its conjugation area. On the other hand, the strong Zn—N ('pyridine-like') bond contributes its conjugation area, but only one π-electron to slightly increase the conjugation area. Therefore, the charge transfer from N to both Zn and C nuclei occurs to a different extent upon vitrification, causing an increase in the conjugation area of the entire tetrahedral units in (Figure 5f). Upon hot-pressing, the framework structure of MQG becomes more defective and denser, accompanied by a reduced intermediate-range structural hindrance (decreased T_g) and a decreased pore size [20]. This induces LLCT in the framework, resulting in the enhancement and broadening of the weak broad emission. Upon annealing at 673 K for 30 min, the pressing-induced structural defects in HPG recover via strengthening of the Zn—N ('pyrrole-like') bond and increasing intermediate-range structural connectivity (increased T_g). Therefore, this annealing opens some new channels for increasing the possibility of LLCT in the glass framework, leading to the formation of some new *p*-orbitals between LUMO and HOMO with reduced bandgap energy (E_g). Consequently, the PL peaks for HPG show a redshift after annealing at 673 K for 30 min (Figure 2e).

Figure 5d,e shows the dependence of the PL peak redshift (under excitation from 360 to 410 nm) on the annealing temperature (T_a) for 30 min duration in MQG and HPG samples, respectively. The annealing temperature-dependent PL spectra and peak positions of MQG and HPG, excited from 360 to 410 nm, are shown in

Figures S28 and S29. The PL peak redshift in MQG only slightly increases with increasing T_a and then sharply increases above a critical T_a, i.e., $1.07T_g$ (633 K) (Figure 5d). In contrast, in the case of HPG, the PL peak position sharply increases with T_a above $1.03T_g$ (613 K) (Figure 5e). That is, the sharp redshift of PL in MQG occurs at a T_a that is 20 K higher than that in HPG, implying that HPG undergoes a higher degree of distortion of the intermediate-range structure (around 0.5–2 nm) compared with MQG. The activation energy for the relaxation (α relaxation) of the distorted structure toward a less distorted structure is lowered by hot-pressing, and hence, a lower T_a is needed for relaxing HPG compared to MQG. Figure S30 shows the evolution of the PL peak position of MQG with varying the annealing time at $1.13T_g$ (673 K) under 375 and 410 nm excitation. It is revealed that the PL peaks under 375 and 410 nm excitation exhibit a pronounced redshift with extending the annealing time up to 10 min, and then remain nearly unchanged up to 60 min. However, an annealing duration of 30 min is chosen in this work to achieve the maximum redshift necessary for cold-white LED fabrication.

The existence of the critical T_a for causing the sharp redshift in PL could be interpreted in terms of relaxation kinetics. The critical T_a of 633 K for MQG corresponds to the viscosity of $10^{8.5}$ Pa·s, as determined by extrapolating the literature viscosity-temperature data using the Mauro-Yue-Ellison-Gupta-Allan (MYEGA) model [18, 39]. At this viscosity, the distorted intermediate-range structure has a high probability of fulfilling the kinetic (diffusional) condition for rearranging itself to a less distorted state during annealing for a certain period. Such structural rearrangement should be concomitant with the translational and rotational motions of the organic linkers toward energetically favorable positions. During such structural rearrangement, a small amount of undercoordinated Zn and N ('pyrrole-like') atoms in free organic linkers, generated during vitrification and hot pressing, should be re-coordinated via forming stable Zn—N ('pyrrole-like') bonds with a slightly higher binding energy [40–43]. The strengthening of the Zn—N bond is inferred by the enhancement of the correlations of the Zn—N bonds as demonstrated by the $\Delta G(r)$ curves of HPG in Figure 4g and Figure S24. This might increase the possibility of the energy transfer from N to Zn, thereby enlarging the conjugation domains of π electrons within the *p*-orbital of the individual linker [44].

More importantly, the structural defects are recovered to form a relaxed glass network, thereby reducing the distances between linkers and increasing the probability of LLCT to tailor the π electrons transition in the *p*-orbital, inducing a redshift of the broadband PL peak (Figure 5f). Consequently, the structural relaxation upon annealing above critical T_a reduces both enthalpy and potential energy in MQG and HPG (Figure 5g), resulting in a slightly yellow shade in appearance (Figure 1b). For the above reasons, the extent of the redshift of PL increases with T_a above $1.03T_g$ and $1.07T_g$ for HPG and MQG, respectively. To further improve the performance of the MOF glass-based LEDs, the optimal T_a still needs to be identified, which can maximize their PL redshift. However, it is important to note that the upper limit of T_a should not exceed the decomposition temperature of MOF glasses. The PLQY of the MOF glass could be further improved by densifying the framework structure through hot-pressing and thereby suppressing the non-radiative transfer of photons. Furthermore, introducing the mixed-node and mixed-ligand effect into MOF glasses could be another route to enhance the PLQY. Beyond improving the LED performance of MOF glasses, it is also important to explore the applications of the LEDs, which are fabricated by using metal–organic hybrid glasses and inorganic–organic hybrid glasses through our pressurization-annealing approach [45–49].

3 | Conclusions

The broadband white light emission of ZIF-62 was observed through the vitrification-pressurization-annealing approach. In contrast, ZIF-62 crystal exhibited both the strong narrowband ultraviolet light emission and the weak broadband visible light emission. The weak broadband visible light emission was enhanced by vitrification, hot-pressing, and annealing. Moreover, a significant redshift was induced by annealing at a temperature above $1.07T_g$. These phenomena were attributed to the decrease in the bandgap caused by enhancing LLCT. The LLCT could result from an extension of the conjugation area from the aromatic moieties of Im and BIm rings to the weak Zn—N ('pyrrole-like') bond. The enhancement of the Zn—N interactions was verified by high-energy synchrotron X-ray diffraction measurements.

Based on the above-mentioned results, we fabricated the broadband white LEDs using the ZIF-62 glass that was annealed at $1.13T_g$ (673 K) for 30 min. The annealed glass exhibited a high internal PLQY of 12.2%. The resultant LED exhibited a luminous efficacy of 4.2 lm/W and retained 36.8% of its original luminous efficacy after 72 h of continuous operation. Therefore, the optimally processed ZIF glasses are promising candidates for developing high-performance solid-state white LEDs.

Acknowledgements

We thank Wessel M. W. Winter and Sabyasachi Sen for helpful discussions. Part of this work was performed at the National High Magnetic Field Laboratory (NHMFL) in Florida, USA, which is funded by the U.S. National Science Foundation (DMR-2128556) and the State of Florida. We acknowledge the Carlsberg Foundation (Grant No. CF21-0371) for funding the STA 449 F3 ASC used in this work and the Villum Fonden (Grant No. 58844) for conducting TEM experiments. Part of this work was financially supported by the Self-deployment Project Research Program of Haixi Institutes (CXZX-2022-GH11), Chinese Academy of Sciences, China. We also acknowledge the P02.1 beamline (Proposal No. I-20240507) at PETRA III, Deutsches Elektronen-Synchrotron (DESY) in Hamburg, Germany and i15 beamline (Proposal No. CY39002) at Diamond Light Source (DLS) in Didcot, United Kingdom.

Conflicts of Interest

The authors declare no conflicts of interest.

Data Availability Statement

The data that support the findings of this study are available from the corresponding author upon reasonable request.

References

1. P. Pust, V. Weiler, C. Hecht, et al., "Narrow-Band Red-Emitting $Sr[LiAl_3N_4]:Eu^{2+}$ as a Next-Generation LED-Phosphor Material," *Nature Materials* 13 (2014): 891–896, https://doi.org/10.1038/nmat4012.

2. X. Huang, "Red Phosphor Converts White LEDs," *Nature Photonics* 8 (2014): 748–749, https://doi.org/10.1038/nphoton.2014.221.

3. H. Zhu, C. C. Lin, W. Luo, et al., "Highly Efficient Non-Rare-Earth Red Emitting Phosphor for Warm White Light-Emitting Diodes," *Nature Communications* 5 (2014): 4312, https://doi.org/10.1038/ncomms5312.

4. F. Nie and D. Yan, "Supramolecular Glass: A New Platform for Ultralong Phosphorescence," *Science China Materials* 67 (2024): 3531–3536, https://doi.org/10.1007/s40843-024-3119-5.

5. H. Tsai, S. Shrestha, R. A. Vilá, et al., "Bright and Stable Light-Emitting Diodes Made With Perovskite Nanocrystals Stabilized in Metal–Organic Frameworks," *Nature Photonics* 15 (2021): 843–849, https://doi.org/10.1038/s41566-021-00857-0.

6. D. Zhang, W. Xiao, C. Liu, et al., "Highly Efficient Phosphor-Glass Composites by Pressureless Sintering," *Nature Communications* 11 (2020): 1–8.

7. Z. Li, D. Zhou, Y. Yang, P. Ren, and J. Qiu, "Adjustable Multicolor Up-Energy Conversion in Light-Luminesce in $Tb^{3+}/Tm^{3+}/Yb^{3+}$ Co-Doped Oxyfluoride Glass-Ceramics Containing Ba_2LaF_7 Nanocrystals," *Scientific Reports* 7 (2017): 1–11.

8. X. Yang and D. Yan, "Direct White-Light-Emitting and Near-Infrared Phosphorescence of Zeolitic Imidazolate Framework-8," *Chemical Communications* 53 (2017): 1801–1804, https://doi.org/10.1039/C6CC09706E.

9. R. Gao, M. S. Kodaimati, and D. Yan, "Recent Advances in Persistent Luminescence Based on Molecular Hybrid Materials," *Chemical Society Reviews* 50 (2021): 5564–5589, https://doi.org/10.1039/D0CS01463J.

10. K. S. Park, Z. Ni, A. P. Côté, et al., "Exceptional Chemical and Thermal Stability of Zeolitic Imidazolate Frameworks," *Proceedings of the National Academy of Sciences* 103 (2020): 10186–10191, https://doi.org/10.1073/pnas.0602439103.

11. Y. Wang, H. Jin, Q. Ma, et al., "A MOF Glass Membrane for Gas Separation," *Angewandte Chemie International Edition* 59 (2020): 4365–4369.

12. Y. Zhao, S.-Y. Lee, N. Becknell, O. M. Yaghi, and C. A. Angell, "Nanoporous Transparent MOF Glasses With Accessible Internal Surface," *Journal of the American Chemical Society* 138 (2016): 10818–10821, https://doi.org/10.1021/jacs.6b07078.

13. Z. Yang, Y. Belmabkhout, L. N. McHugh, et al., "ZIF-62 Glass Foam Self-Supported Membranes to Address CH_4/N_2 Separations," *Nature Materials* 22 (2023): 888–894, https://doi.org/10.1038/s41563-023-01545-w.

14. A. Bavykina, N. Kolobov, I. S. Khan, J. A. Bau, A. Ramirez, and J. Gascon, "Metal-Organic Frameworks in Heterogeneous Catalysis: Recent Progress, New Trends, and Future Perspectives," *Chemical Reviews* 120 (2020): 8468–8535.

15. C. Gao, Z. Jiang, S. Qi, et al., "Metal-Organic Framework Glass Anode With an Exceptional Cycling-Induced Capacity Enhancement for Lithium-Ion Batteries," *Advanced Materials* 34 (2022): 1–13, https://doi.org/10.1002/adma.202110048.

16. T. D. Bennett, J.-C. Tan, Y. Yue, et al., "Hybrid Glasses From Strong and Fragile Metal-Organic Framework Liquids," *Nature Communications* 6 (2015): 1–7, https://doi.org/10.1038/ncomms9079.

17. J. Song, L. Frentzel-Beyme, R. Pallach, et al., "Modulating Liquid–Liquid Transitions and Glass Formation in Zeolitic Imidazolate Frameworks by Decoration With Electron-Withdrawing Cyano Groups," *Journal of the American Chemical Society* 145 (2023): 9273–9284, https://doi.org/10.1021/jacs.3c01933.

18. A. Qiao, T. D. Bennett, H. Tao, et al., "A Metal-Organic Framework With Ultrahigh Glass-Forming Ability," *Science Advances* 4 (2018): 1–8, https://doi.org/10.1126/sciadv.aao6827.

19. S.-X. Peng, Z. Yin, T. Zhang, Q. Yang, H.-B. Yu, and M.-H. Zeng, "Vibration Assisted Glass-Formation in Zeolitic Imidazolate Framework," *The Journal of Chemical Physics* 157 (2022): 104501, https://doi.org/10.1063/5.0109885.

20. A. Qiao, S. S. Sørensen, M. Stepniewska, et al., "Hypersensitivity of the Glass Transition to Pressure History in a Metal–Organic Framework Glass," *Chemistry of Materials* 34 (2022): 5030–5038, https://doi.org/10.1021/acs.chemmater.2c00325.

21. J. Hou, P. Chen, A. Shukla, et al., "Liquid-Phase Sintering of Lead Halide Perovskites and Metal-Organic Framework Glasses," *Science* 374 (2021): 621–625, https://doi.org/10.1126/science.abf4460.

22. R. Grau-Crespo, A. Aziz, A. W. Collins, et al., "Modelling a Linker Mix-and-Match Approach for Controlling the Optical Excitation Gaps and Band Alignment of Zeolitic Imidazolate Frameworks," *Chemical Communications* 55 (2016): 16012–16016.

23. M. Gustafsson and X. Zou, "Crystal Formation and Size Control of Zeolitic Imidazolate Frameworks With Mixed Imidazolate Linkers," *Journal of Porous Materials* 20 (2013): 55–63, https://doi.org/10.1007/s10934-012-9574-1.

24. R. N. Widmer, G. I. Lampronti, S. Anzellini, et al., "Pressure Promoted Low-Temperature Melting of Metal–Organic Frameworks," *Nature Materials* 18 (2019): 370–376, https://doi.org/10.1038/s41563-019-0317-4.

25. G. Kumari, K. Jayaramulu, T. K. Maji, and C. Narayana, "Temperature Induced Structural Transformations and Gas Adsorption in the Zeolitic Imidazolate Framework ZIF-8: A Raman Study," *The Journal of Physical Chemistry A* 117 (2013): 11006–11012, https://doi.org/10.1021/jp407792a.

26. Z. Li, C. Chen, W. Shen, et al., "The Transformation From Translucent Into Transparent Rare Earth Ions Doped Oxyfluoride Glass-Ceramics With Enhanced Luminescence," *Advanced Optical Materials* 10 (2022): 2102713, https://doi.org/10.1002/adom.202102713.

27. S. Liu, Z.-R. Wang, X. Lin, et al., "Structural Comparisons, Fluorescence Properties, and Glass-to-Crystal Transformations of Heat-Cooled and Melt-Quenched Zeolitic Imidazolate Framework Glass," *Angewandte Chemie International Edition* 63 (2024): 18574–18580.

28. Y. Zou, S. Abednatanzi, P. G. Derakhshandeh, et al., "Red Edge Effect and Chromoselective Photocatalysis With Amorphous Covalent Triazine-Based Frameworks," *Nature Communications* 13 (2022): 1–13, https://doi.org/10.1038/s41467-022-29781-9.

29. O. Smirnova, R. Sajzew, S. J. Finkelmeyer, et al., "Micro-Optical Elements From Optical-Quality ZIF-62 Hybrid Glasses by Hot Imprinting," *Nature Communications* 15 (2024): 5079, https://doi.org/10.1038/s41467-024-49428-1.

30. A. Birkel, K. A. Denault, N. C. George, et al., "Rapid Microwave Preparation of Highly Efficient Ce^{3+}-substituted Garnet Phosphors for Solid state White Lighting," *Chemistry of Materials* 24 (2012): 1198–1204, https://doi.org/10.1021/cm3000238.

31. Y.-L. Li, Y.-R. Huang, and Y.-H. Lai, "Efficiency Droop Behaviors of InGaN/GaN Multiple-Quantum-Well Light-Emitting Diodes With Varying Quantum Well Thickness," *Applied Physics Letters* 91 (2007): 181113, https://doi.org/10.1063/1.2805197.

32. R. S. K. Madsen, A. Qiao, J. Sen, et al., "Ultrahigh-Field ^{67}Zn NMR Reveals Short-Range Disorder in Zeolitic Imidazolate Framework Glasses," *Science* 367 (2020): 1473–1476, https://doi.org/10.1126/science.aaz0251.

33. K. Bouchmella, S. G. Dutremez, B. Alonso, and F. Mauri, "^{1}H, ^{13}C, and ^{15}N Solid-State NMR Studies of Imidazole- and Morpholine-Based Model Compounds Possessing Halogen and Hydrogen Bonding Capabilities," *Crystal Growth & Design* 8 (2008): 3941–3950, https://doi.org/10.1021/cg700975v.

34. Z. An, C. Zheng, Y. Tao, et al., "Stabilizing Triplet Excited States for Ultralong Organic Phosphorescence," *Nature Materials* 14 (2015): 685–690, https://doi.org/10.1038/nmat4259.

35. J. Perego, C. X. Bezuidenhout, I. Villa, et al., "Highly Luminescent Scintillating Hetero-Ligand MOF Nanocrystals With Engineered Stokes shift for Photonic Applications," *Nature Communications* 13 (2022): 1–10, https://doi.org/10.1038/s41467-022-31163-0.

36. X. Guo, L. Liu, Y. Xiao, Y. Qi, C. Duan, and F. Zhang, "Band Gap Engineering of Metal-Organic Frameworks for Solar Fuel Productions," *Coordination Chemistry Reviews* 435 (2021): 213785, https://doi.org/10.1016/j.ccr.2021.213785.

37. M. A. Ali, J. Ren, T. Zhao, et al., "Broad Mid-Infrared Luminescence in a Metal–Organic Framework Glass," *ACS Omega* 4 (2019): 12081–12087, https://doi.org/10.1021/acsomega.9b01559.

38. X. Ge, P. Lai, C. Shi, et al., "Unconventional Floppy Network Structures in Titanate Glasses," *Acta Materialia* 253 (2023): 118953, https://doi.org/10.1016/j.actamat.2023.118953.

39. J. C. Mauro, Y. Yue, A. J. Ellison, P. K. Gupta, and D. C. Allan, "Viscosity of Glass-Forming Liquids," *Proceedings of the National Academy of Sciences* 106 (2009): 19780–19784, https://doi.org/10.1073/pnas.0911705106.

40. D. S. Sholl and R. P. Lively, "Defects in Metal–Organic Frameworks: Challenge or Opportunity?," *The Journal of Physical Chemistry Letters* 6 (2015): 3437–3444, https://doi.org/10.1021/acs.jpclett.5b01135.

41. T. D. Bennett, A. K. Cheetham, A. H. Fuchs, and F.-X. Coudert, "Interplay Between Defects, Disorder and Flexibility in Metal-Organic Frameworks," *Nature Chemistry* 9 (2016): 11–16, https://doi.org/10.1038/nchem.2691.

42. T. Du, S. Li, S. Ganisetti, M. Bauchy, Y. Yue, and M. M. Smedskjaer, "Deciphering the Controlling Factors for Phase Transitions in Zeolitic Imidazolate Frameworks," *National Science Review* 11 (2024), https://doi.org/10.1093/nsr/nwae023.

43. R. Gaillac, P. Pullumbi, K. A. Beyer, et al., "Liquid Metal–Organic Frameworks," *Nature Materials* 16 (2017): 1149–1154, https://doi.org/10.1038/nmat4998.

44. Z. Li, Z. Wang, H. Zhang, et al., "Zeolitic Imidazolate Framework Glasses Emit White Light," *arXiv* (2025): arXiv:2508.09552.

45. F. Nie and D. Yan, "Molecular Glass From Solution Self-Assembly," *Accounts of Chemical Research* 58 (2025): 3010–3020, https://doi.org/10.1021/acs.accounts.5c00425.

46. B. Zhou and D. Yan, "Glassy Inorganic-Organic Hybrid Materials for Photonic Applications," *Accounts of Chemical Research* 57 (2024): 1950–1976.

47. B. Zhou, Z. Qi, and D. Yan, "Highly Efficient and Direct Ultralong All-Phosphorescence from Metal-Organic Framework Photonic Glasses," *Angewandte Chemie International Edition* 61 (2022): 202208735.

48. M. Dai, B. Zhou, and D. Yan, "Rare Earth Single-Atomic Hybrid Glasses for Near-Infrared II Optical Waveguides," *Angewandte Chemie International Edition* 64 (2025): 202505322.

49. F. Nie, K.-Z. Wang, and D. Yan, "Supramolecular Glasses With Color-Tunable Circularly Polarized Afterglow Through Evaporation-Induced Self-Assembly of Chiral Metal–Organic Complexes," *Nature Communications* 14 (2023): 1654, https://doi.org/10.1038/s41467-023-37331-0.

Supporting Information

Additional supporting information can be found online in the Supporting Information section.

Supporting File 1: adma72968-sup-0001-SuppMat.docx.

Supporting File 2: adma72968-sup-0002-Movie S1.mp4.

Supporting File 3: adma72968-sup-0003-Movie S2.mp4.